# Aspects of Tidal Stream Turbine Modelling in the Natural Environment Using a Coupled BEM-CFD Model

M.Edmunds, R.Malki, A.J.Williams, I.Masters, T.N.Croft

*Marine Energy Research Group, College of Engineering, Swansea University, Wales, UK, SA2 8PP.*

## Abstract

The problem of designing the optimal array of tidal stream turbines for the generation of marine renewable energy from the ocean, raises a number of questions about the distribution and layout of turbines in relation to the local bathymetry. The computational overhead of modelling such problems may be significant and costly. This paper aims to clarify the effects of particular phenomena associated with modelling tidal stream turbine arrays. To achieve this we use a RANS computational fluid dynamics model with an embedded blade element actuator disk to investigate various aspects of this problem, while maintaining reduced computational overhead.

A study of axially aligned turbines, with each in the wake shadow of the previous turbine shows uniform effects for a 20 diameters downstream spacing, but more complex interaction for 10 diameters spacing. Investigation of the significance of inclusion of the nacelle and tower geometry in a CFD model shows that effects are negligible beyond six diameters downstream. An array of transverse contrarotating turbines are considered, where a device is placed close to and in the wake of a pair of upstream devices. Rotational direction has minimal effect on the power generated, but different turbulence is seen in the wake. Finally, marine currents around a headland are modelled and a single row fence of turbines is placed offshore from the headland at various blockage ratios. Power performance estimates and downstream wakes are created and they show increased power per device and improved total power production as the blockage ratio rises from 0.13 to 0.20. Additionally, the authors use stream surface techniques to visualise the flow which can give new insights to the physical processes observed.

*Keywords:*
bathymetry, tidal, turbines, marine, renewable, RANS, BEM, CFD, wake, shadow, nacelle, tower, contrarotating, turbulence, power, headland, fence, blockage, stream surface.

## 1. Introduction

Tidal stream renewable energy is becoming a viable source of electricity as part of a diversified low carbon energy mix. Across the world sites are being identified where the currents are sufficiently strong to enable economically attractive levels of energy extraction. Grid connected prototype devices are generating power and industry attention is turning to the development of arrays of multiple tidal turbine rotors.

Academic interest in the sector is growing in parallel to the growth of industrial investment. A large number of papers have now been published, ranging from device design, through environmental impact, to the hydrodynamic performance of devices, individually and in arrays. It is the last of these issues that this paper seeks to inform. There are numerous approaches for numerical modelling of tidal stream turbines and we discuss some of these below. Each methodology has advantages and disadvantages, with the main balance being a trade off between detailed simulation of the physics and the computational time and resources required to achieve a result.

At the largest scale, oceanographic models have been modified to include turbine arrays and the effects of energy extraction is considered. With grid cells between 20-2000m in size, turbines are typically included as sub-grid modification, with the most naive implementation being a simple increase in local bed friction.

Issues of interest at this scale include sediment transport ([1]) and the combined features of waves, currents and sediments ([2]). At the smallest and most detailed scale, computational models of individual turbines have been created and validated against experiments ([3], [4], [5]). Such models can resolve turbine performance characteristics as well as blade tip vortices and wake propagation. Techniques generally include a moving mesh that is resolved to the geometry of the blade, using either a Reynolds Averaged Navier Stokes ([6]) or Large Eddy Solver ([7]) approach. Extensions to these models include the depth variation of inlet velocity ([6], [7]) and considerations of blade stresses through fluid structure interaction ([8]).

Between these two levels of detail are energy source models, where the geometry of the rotor is abstracted into an energy source/sink term. [9] uses actuator disks to represent each rotor and investigates the positive blockage that can be achieved by closely spaced rotors. [10] abstract this further into what is effectively an actuator fence and consider the interactions between the fence and a headland. Also of interest are actuator line approaches, where a rotating line of energy sinks represents each of the rotor blades at a sub grid scale. The method was developed by [11].

This paper uses the Blade Element Momentum Computational Fluid Dynamics (BEM-CFD) method developed by [12], which is similar in approach to [13] and [14]. This combines a finite volume multiphysics CFD code, Physica ([15]) with an additional energy source term to represent the rotor. Although similar to the more familiar actuator disk approach ([9]), the source is based on the classical Blade Element Momentum Theory ([16]) and emulates the effects of the blade twist, chord, lift and drag characteristics. The method requires reasonable, but not excessive, computational requirements. Although the method can produce transient flow results, it is normally used to create steady state models, which is in keeping with the time averaged nature of the BEM disks. Transient flow features can be identified through the various turbulence parameters. The model has successfully been used to consider the relationship between wake length and inflow velocity ([17]), and accelerating flows ([18]). [19] considers arrays of turbines and reports validation for three turbines against the work of [20] before considering 14 turbine arrays.

Flow visualisation is an important and powerful means for analysing, exploring and communicating simulation or experimental results. Flow visualisation results can differ in their complexity, quality and style. Stream surfaces have become increasingly popular in recent years, and have important inherent characteristics that can enhance the visual perception of complex flow structures. Lighting and shading reinforce the perception of shape and depth, images or textures can be mapped to the surface primitives providing additional visual information, colour and transparency can be used to convey additional data attributes. Surfaces in general are able to not only capture the features within the flow, but also have the inherent ability to convey further information about the local attributes of the flow. This combined with the reduction in visual clutter when compared to using glyphs or streamlines, significantly enhances the utility of surfaces for practitioners.

A stream surface is the integration of a one dimensional curve through 3D steady flow. The resulting surface is everywhere tangent to the local flow. Since there is no normal component of the velocity along stream surfaces, thus they are useful for separating distinct regions of similar flow behaviour. In practical applications a discretised approximation of the stream surface is constructed by integrating discretised seeding curves through the vector field, [21], [22], and [23].

The development of such flexible modelling capability provides tidal stream project developers with a modelling and visualisation tool that can be used to consider various aspects of the flow around turbines, which is particularly of interest for the optimal positioning of arrays of devices. This paper is therefore motivated by different aspects of array design that have been considered in the literature or have been important in the authors experience. The first aspect of interest is the spacing of turbines downstream from each other as investigated by [24] and extended here. The second is the continued debate about the performance of contra-rotating arrays of turbines, even though it has been investigated by [6] and considering that the downstream swirl only accounts for a few percent of the total energy exchange at the rotor. The third is the computational overhead of modelling flow around turbine nacelles, removing the nacelle provides significant computational efficiency and this work investigates the impact of this on performance estimates. The fourth aspect is the influence of local topography. Inspired by [10], a model of a tidal fence located next to a headland is reported. All of these aspects provide greater insight into improved turbine array development.

This article starts with an overview of the numerical scheme, together with descriptions of the various computational cases. Each of the results is discussed in turn and finally conclusions bring all the aspects together.

## 2. Numerical Modelling

### 2.1. The Coupled BEM-CFD Model

#### 2.1.1. Governing Equations

The CFD model requires the solution of the Navier Stokes equations representing the conservation of mass and momentum. These equations are expressed as follows:

$$\nabla \cdot (\rho \underline{u}) = 0 \tag{1}$$

$$\nabla \cdot (\rho \underline{u} u_i) = -\partial p / \partial x_i + \nabla \cdot (\mu_{lam} + \mu_t) \nabla \rho u_i + S_i \tag{2}$$

where $\rho$ is the density, $u_i$ is the $i$th component of the velocity vector, $u_{lam}$ and $u_t$ are the laminar and turbulent dynamic viscosities respectively, and $S_i$ includes an additional source representing the moving rotor.

The effect of turbulence on the mean flow, at the sub grid level, is resolved through the $k-\epsilon$ model [25]. This is the most widely used turbulence model due to its relative simplicity, modest computational cost, and stability. The main limitation of this model is that the turbulence viscosity is calculated using a single length scale. In reality turbulence diffusion occurs at a wide range of length and time scales. This shortfall is addressed by the $k-\epsilon$ RNG model which uses statistical methods to account for the different scales of motion. These models assume turbulence to be isotropic in nature. This is usually a reasonable approximation, however in rotational flows the eddies can become anisotropic.

Higher order turbulence models, such as the Reynolds stress model or large eddy simulation, can produce better predictions of the turbulence structure. However, these models require greater computational expense. The focus on performance of turbine rotors, rather than flow structures of the highly turbulent near wake region immediately downstream of the device, justifies the use of the $k-\epsilon$ model. In this model two equations are solved; for the first $k$ represents the energy contained within the turbulence, and for the second $\epsilon$ represents the dissipation of this energy. The equations for the transport of these variables are similar in form to the momentum equations:

$$\nabla \cdot (\rho \underline{u} k) = \nabla \cdot (\mu_{lam} + \mu_t / \sigma_k) \nabla k + \mu_t G - \rho \epsilon \tag{3}$$

$$\nabla \cdot (\rho \underline{u} \epsilon) = \nabla \cdot (\mu_{lam} + \mu_t / \sigma_\epsilon) \nabla \epsilon + \mu_t G - \rho \epsilon + \epsilon / k (C_{1\epsilon} \mu_t G - C_{2\epsilon} \rho \epsilon) \tag{4}$$

These equations are used to calculate a turbulent viscosity:

$$\mu_t = \rho C_\mu k^2 / \epsilon \tag{5}$$

In Equations 3, 4, and 5; $\sigma_k$, $\sigma_\epsilon$, $C_{1\epsilon}$, $C_{2\epsilon}$, and $C_\mu$ are taken to be constants, and $G$ represents the turbulent generation rate. The viscosity components of the $k$ and $\epsilon$ momentum equation diffusion terms, are effectively the sum of the laminar and turbulent viscosities.

#### 2.1.2. Rotor Representation

The influence of a turbine with multiple blades is time averaged over a significant time interval for the blade element actuator disk and therefore the influence of the blades becomes evenly distributed over the blade area. An alternative way of considering this approximation is an infinite number of infinitely thin blades within the swept area. The rotor applies the same force to all locations at the same radial distance from the rotor centre. Magnitudes of such forces are a function of blade geometry, and its hydrodynamic

3

(a) Rotor discretisation schematic.

(b) Blade element schematic.

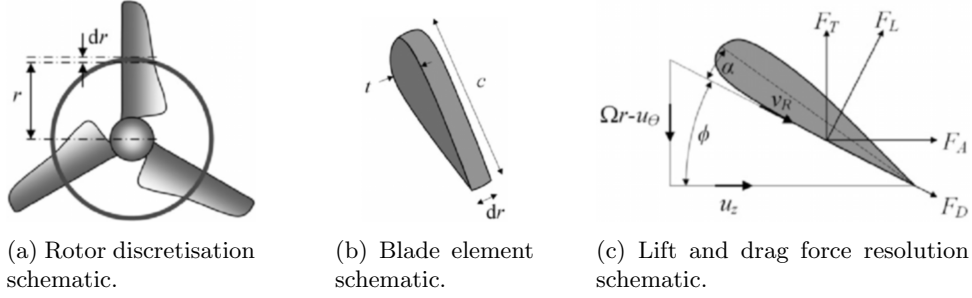(c) Lift and drag force resolution schematic.

Figure 1: Blade element method rotor discretisation scheme.

properties. These forces are characterised by the variations in lift and drag coefficients as a result of the blade chord length, twist angle, rotational speed and the consequent angle of attack.

Source terms, which are functions of radial and axial position, are applied to each of the momentum equations representing the force of the turbine blades acting on the fluid. The physical characteristics of the blade are introduced through the source terms in contrast to being resolved using an exact geometry. Conversely, because of the Reynolds averaged nature of the solution, it fails to resolve any transient flow features due to blade position. This includes tip vortices, the laminar to turbulent transition along the blade surface, flow separation, and turbulence generation along the downstream part of the hydrofoil.

Figure 1a shows how a three bladed turbine is discretised for use with the blade element method. The blade properties are determined at radius $r_i$, and then averaged over 360°. This process is repeated for each blade element over the interval $[r_0, r_{max}]$. In Figure 1b, a close up schematic of a blade element is illustrated. The schematic indicates the element chord length $c$, the element thickness $t$, and the element radial length $dr$.

The fluid applies axial and tangential forces to each element as illustrated in Figure 1c. Here $F_T$ is the torque and $F_A$ represents the axial force. The lift and drag forces, $F_L$ and $F_D$ respectively, are dependent on the angle of attack $\alpha$. This is the angle between the blade element and the resultant velocity $v_R$, as shown in Figure 1c.

Based on the approach in [16], an axial force on a blade element can be defined as follows:

$$F_A = F_L sin\phi + F_D cos\phi \tag{6}$$

and the tangential force on a blade element, which is equal to the torque/radius, i.e. $dF_T/r$, can be defined as:

$$F_T = F_L cos\phi - F_D sin\phi \tag{7}$$

where $\phi$ is the flow inclination angle defined by:

$$\phi = tan^{-1}((\Omega r - u_\theta)/u_z) \tag{8}$$

Here $u_\theta$ and $u_z$ are the tangential and axial velocities respectively. $\Omega$ is angular velocity $[rad/s]$. The variation in lift force $dF_L$, and drag force $dF_D$, acting along the blade radius are given as follows:

$$dF_L = \rho |v_R|^2 C_L cdr/2 \tag{9}$$

$$dF_D = \rho |v_R|^2 C_D cdr/2 \tag{10}$$

Here $C_L$ and $C_D$ are the lift and drag coefficients respectively, and:

$$|v_R|^2 = u_z^2 + (\Omega r - u_\theta)^2 \tag{11}$$

4

Substituting Equations 9 and 10 into Equations 6 and 7 gives the following:

$$S_z = dF_A$$
$$= \rho|v_R|^2 cdr(C_L sin\phi + C_D cos\phi)/2 \qquad (12)$$

$$S_\theta = dF_T$$
$$= \rho|v_R|^2 cdr(C_L cos\phi - C_D sin\phi)/2 \qquad (13)$$

which, when resolved to Cartesian components and converted to force per volume, are combined with the momentum equation (Equation 2) as the source term $S_i$. A complete description of the method and validation against tank data is given in [18], and comparisons of the approach against experimental data for 2 and 3 rotors is given in [19].

## 3. Model Definitions

In this paper a number of scenarios related to modelling tidal stream turbines are investigated. The following sections describe the geometries that are considered, and include details relating to the meshes and boundary conditions.

### 3.1. Geometries

The first case that is considered is related to the results of [24] who investigated the performance of an array of turbines aligned linearly along the flow direction. In [24] it is suggested that the power output for any given turbine in the array can be determined by applying a common factor to the power output of the turbine immediately upstream. These conclusions are based on observations of flow recovery for a single turbine.

The hypothesis of [24] is tested here by modelling a four turbine array where the 3-blade, 10 m rotor diameter, turbines have a spacing in the longitudinal direction of 10 diameters and 20 diameters. A schematic of the geometry in the flow direction can be seen in Figure 2. The position and dimensions of the first turbine in these arrays are shown in Figure 3. It should be noted that all the turbines have the same dimensions, and that the turbine model consists of a nacelle and rotor. The width and depth of the channel (200 m and 30 m respectively) have been chosen to ensure that blockage effects are negligible. The second case that is investigated is motivated by the need to model large arrays with sufficient accuracy whilst reducing mesh complexity, and considers the effect that including the supporting structure of a rotor has on modelling performance and wake dynamics. Two single turbine models are considered:

- A rotor, nacelle and tower.

- A rotor.

In each case the turbine structure is located centrally in a channel of width 200 m and depth 30 m, with the 3 blade, 10 m diameter, rotor located 301 m downstream of the inlet, see Figure 4. The total length of the channel is 405 m.

In order to investigate the effects of transverse contrarotation on performance when designing an array layout, a staggered three turbine array geometry is modelled. In this case the turbine geometry consists of a rotor and nacelle. The first row of the array is positioned centrally in a channel 200 m wide, and consists of two turbines with a distance of 15 m between the rotor centres. The second row of the array consists of one turbine which is placed 10 m downstream of the front of the first row as shown in Figure 5. As in the previous cases, the turbines are positioned mid depth in the 30 m deep channel and the rotors have 3 blades with a diameter of 10 m. The layout is similar to an experimental setup reported by [20] and a parametric study of three turbines rotating in the same direction was investigated previously in [19]. The reader is directed to [6] for a blade resolved CFD analysis of contrarotating turbines.
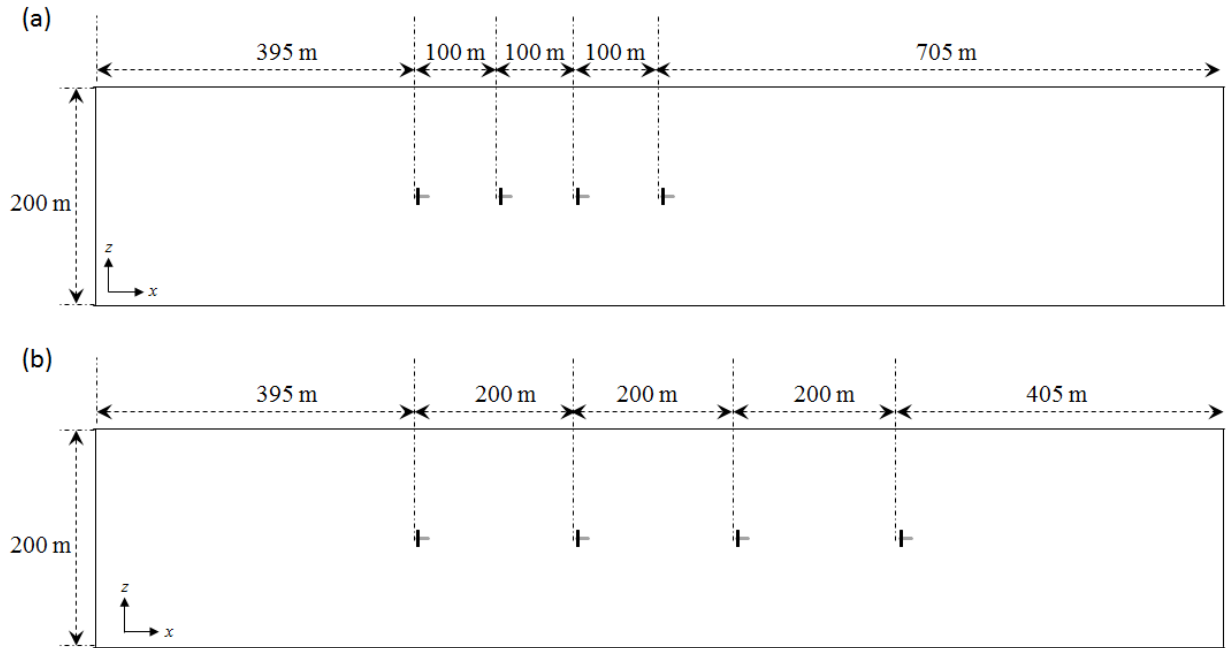
Figure 2: Schematic, in the x-z plane, of four turbine array separated by intervals of (a) 10 diameters and (b) 20 diameters.
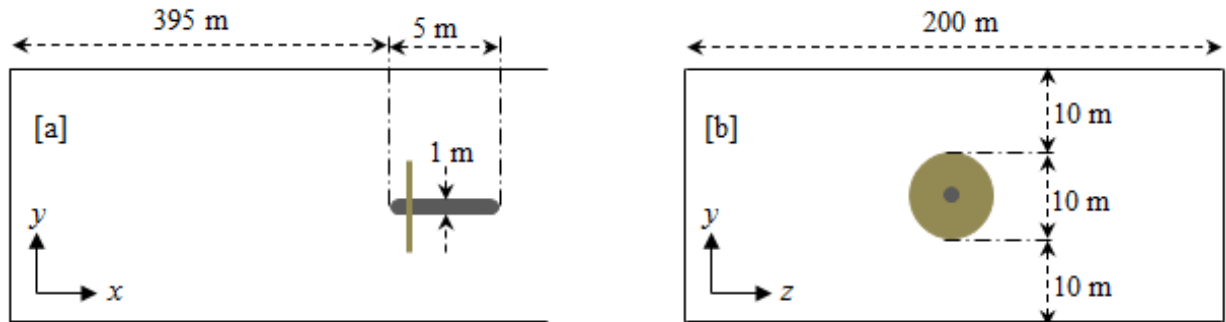


Figure 3: Schematic showing the position of the first rotor and nacelle in the four turbine array models (a) in relation to the inlet boundary in the x-y plane and (b) in the lateral z-y plane.

In the final case, the effect of placing an array of turbines close to a headland is investigated. This is based on research published by [10] where a series of simulations are carried out using a 2D mesh. The aim of this work is to develop a 3D model for the headland case. A schematic of the geometry is presented in Figure 6, and the channel has a constant depth of 30 m. Due to issues related to numbers of mesh elements, the scale of the 3D geometry is smaller than the 2D geometry in [10]. However, the shape of the headland is consistent with that in [10], as is the relative position of the turbine array, and the dimensions of the 3D geometry have been chosen to ensure that blockage effects are neglected. In this set of simulations only the rotor (3 blades, 10 m diameter) is modelled in order to reduce mesh complexity.

### 3.2. Meshing

It is important to ensure that the properties of the rotor blades are captured as accurately as possible within the model. In order to do this a "blade-box" is defined which is an allocated region of the domain that is large enough to encompass the rotor, or, as in the case of a lateral array of turbines, more than one
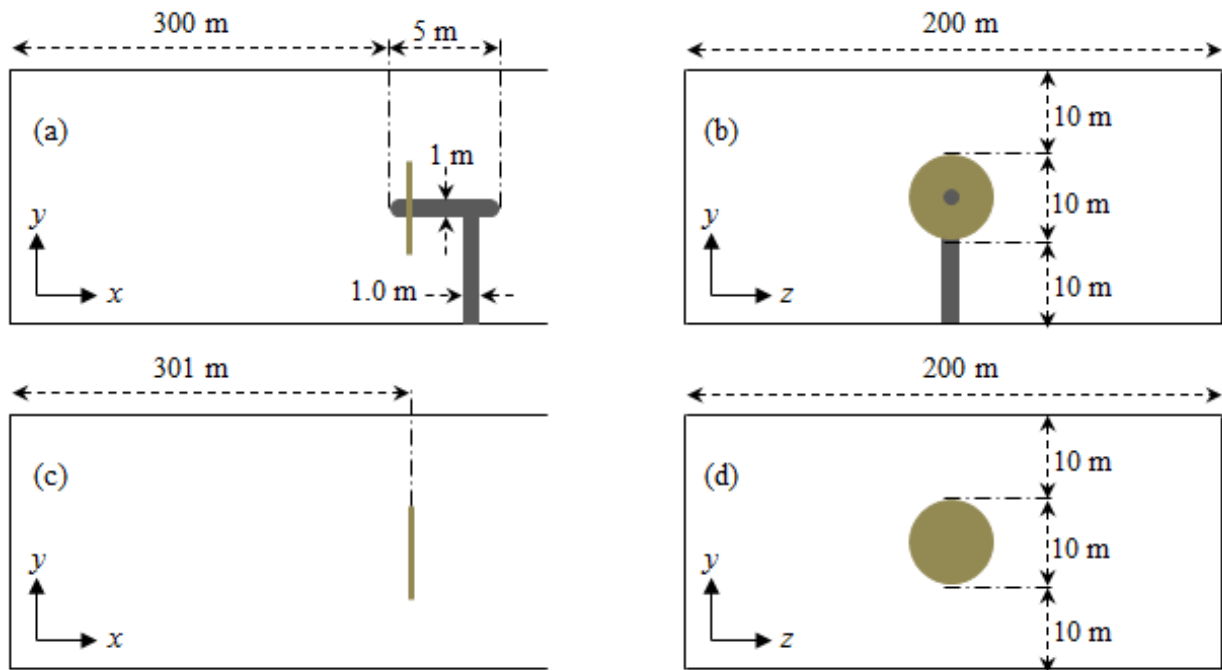
Figure 4: Schematic showing the position of the rotor, nacelle and tower in the single turbine model (a) in relation to the inlet boundary in the x-y plane and (b) in the lateral z-y plane, and the corresponding position of the rotor model (c) in relation to the inlet boundary and (d) in the lateral z-y plane.
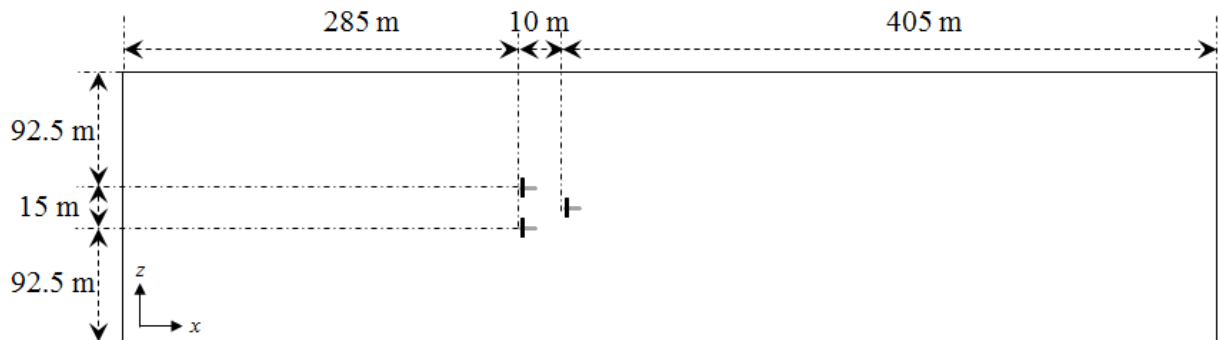


Figure 5: Schematic showing dimensions of geometry in the x-z plane for staggered three turbine array case

rotor. It is important that the mesh within the "blade-box" region is structured as this improves the blade representation. In the cases presented here the meshes for the remainder of the domains are unstructured.

Further information related to the methodology behind the mesh design for the geometries in this study can be found in [12], [18] and [19]. In particular, discussion about mesh sensitivity in the rotor region and the wake region is presented in [12] and [18] respectively. The authors of these works evaluate convergence and mesh dependency of a range of mesh densities. The work concludes that values decreased with increasing mesh resolution along the lateral and vertical directions. Errors ranged between 0.3% and 8.8%. The mesh resolution used here corresponds to an error of 0.4%. Simulations conducted for this study are run for 13,000 iterations, by which point changes to values and coefficients with further iterations are insignificant.

Based on the recommendations in these previous studies, a structured mesh is employed in the blade box region with a resolution of 64 x 64 x 10 elements with cell sizes of 0.2 m x 0.2 m x 0.1 m. An unstructured
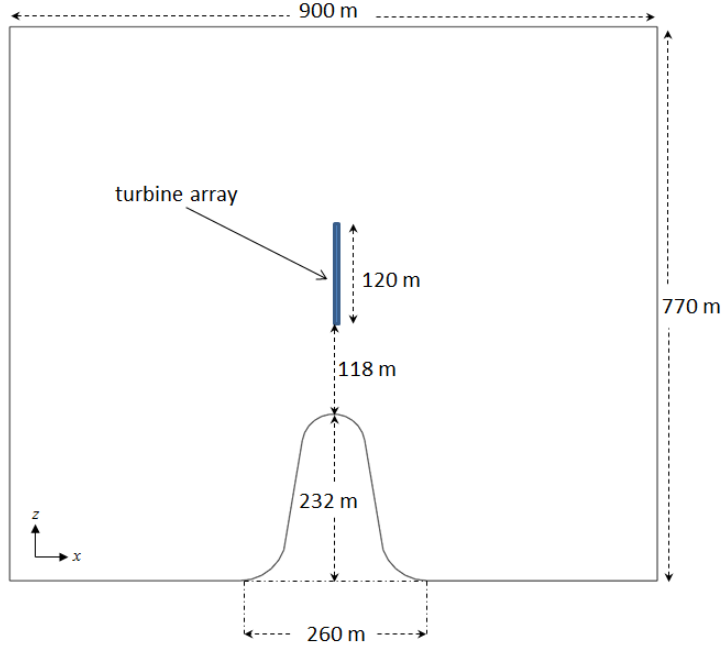
Figure 6: Dimensions of the headland geometry and location of turbine array.

mesh is implemented in the upstream regions with maximum element sizes of 1.0 m between -55 m (55 m upstream of the turbine) and 60 m (60 m downstream of the turbine), except the rotor vicinity of -5 m and 10 m where a maximum element size of 0.5 m was implemented. Beyond 60 m downstream of the rotor, a maximum element size of 2.0 m was implemented, and 4.0 m along the outer boundaries of the model domain. Table 7 contains details about the number of elements contained in each mesh.

| Case | No. of elements |
|---|---|
| Four turbine array, 10 diameter spacing | 8,843,163 |
| Four turbine array, 20 diameter spacing | 10,455,528 |
| Single turbine (tower and nacelle) | 2,984,213 |
| Single turbine (rotor only) | 3,222,157 |
| 3 turbine array | 5,794,534 |
| Headland | 17,403,062 |

Figure 7: The number of mesh elements in the cases considered in this study.

### 3.3. Boundary Conditions

In all the test cases presented in this paper a plug flow inlet velocity condition of 3 m/s in the longitudinal direction (positive $x$ direction) is imposed, with a zero pressure boundary condition on the downstream boundary. No-slip boundary conditions are implemented on the base of the channel and turbine nacelle and tower, where present. For the single turbine, and three and four turbine array geometries, symmetry boundary conditions are imposed on the side and top surfaces of the computational domain. In the headland case a no-slip velocity boundary condition is imposed along the side of the geometry containing the headland feature, while a symmetry boundary condition is implemented on the remaining side and top surface of the domain. In these studies the turbines are operating close to an optimal TSR of 3 based on the local velocity at the rotor.

8

## 4. Results and Discussion

### 4.1. Aspects of a Marine Turbine and Wake

Specifying a marine turbine to effectively extract power from the flow requires some study. The variable speed turbine specified for our work includes a three bladed rotor of 10 meters in diameter [19]. The blade profile, chord, and twist, are specified with consideration of the TSR (Tip Speed Ratio) and $Cp$ profile [19]. In our simulations our blades are designed for optimum operation around a TSR of 3.0, where TSR $= R\Omega/u$, $R$ is blade radius, $\Omega$ is angular velocity, and $u$ is velocity. An example is the headland case where the operating velocities provided a $Cp$ range of approximately 0.42 to 0.44. This indicates an operating condition where the lower and upper bounds are close to optimum. To compute the correct operating conditions for the rotors currently requires an approach of trial and error. This is of particular issue for downstream turbines where it is difficult to predict the velocity profiles at these locations, and thus a number of iterations is required to find the optimum operating condition.

The downstream wake observed behind the turbine structure is characterised by a velocity deficit. As the distance downstream increases, the wake velocity will eventually recover as a result of momentum transfer back into the wake from the turbulent mixing in the shear layer between the free stream and wake regions. As the wake velocity deficit recovers so does the potential to extract power. The wake edge is defined as the contour around and downstream of the turbine where the velocity is 95% of the free stream velocity, [17]. A maximum wake width is observed after the wake recovers to approximately 75% of the free stream velocity, after which the wake tends to dissipate [17]. The wake length is a function of the turbine inlet velocity, and the rate of momentum extraction by the turbine. More formally, the length and width are related to the Reynolds number of the flow as determined by the inlet velocity.

The influence of turbulence intensity on wake recovery extends from the turbulent mixing immediately behind the turbine, propagating both inwards towards the wake axis of rotation, and outwards. This encourages the downstream wake to widen while increasing the recovery of the velocity deficit. This effect is governed by the turbulence intensity in the wake region. The total downstream turbulence intensity is the sum of the ambient (free stream) turbulence intensity, the rotor induced mechanical turbulence intensity, and the wake edge velocity gradient (or shear) generated turbulence intensity as noted by [24]. The wake edge shear generated turbulence intensity is influenced by the increased velocity in the bypass region of the flow. This increased velocity has the effect of increasing the turbulence at the wake boundary, thus improving the wake recovery rate.

### 4.2. Shadowing of Marine Turbines

The trade off between the density of turbines in a given area verses the maximal power extraction per turbine is the subject of analysis in this paper. More specifically, the effect of the shadowing of downstream turbines by upstream rows has on power production, and the optimal interval between turbines. Placement of an additional turbine structure downstream of the first has implications for power production as a result of the velocity deficit. If placed far enough downstream then the velocity deficit will be minimal, and power extraction will be maximal. However, this is impractical as tidal stream sites are of finite size. The power extraction becomes more efficient as the intervals increase. However, a denser arrangement of turbines can extract a greater total quantity of power.

The optimum density for turbine array layout in a given area has been studied by [24], who describe a method for assessing the optimum performance of tidal current turbines arranged in a given area. The authors use this method to assess a $1km^2$ field of turbines arranged in a rectilinear grid. The lateral spacing and downstream intervals are examined at differing densities to find the optimum potential power extraction. An individual turbine is assessed using a coupled RANS-BEM simulation at differing domain widths. The lateral domain boundaries use symmetry (free slip boundary condition) to represent the lateral spacing of turbines at two diameters, four diameters, and six diameters, where the rotors are 20 meters in diameter. The downstream turbine performance is assessed by examining the downstream velocity and feeding this information into the BEM model to evaluate the power extraction at the different intervals.

[24] describe how the accelerated velocity bypassing the rotors can improve the wake recovery rate due to the increased velocity shear at wake boundary. This improves the potential power extraction at downstream
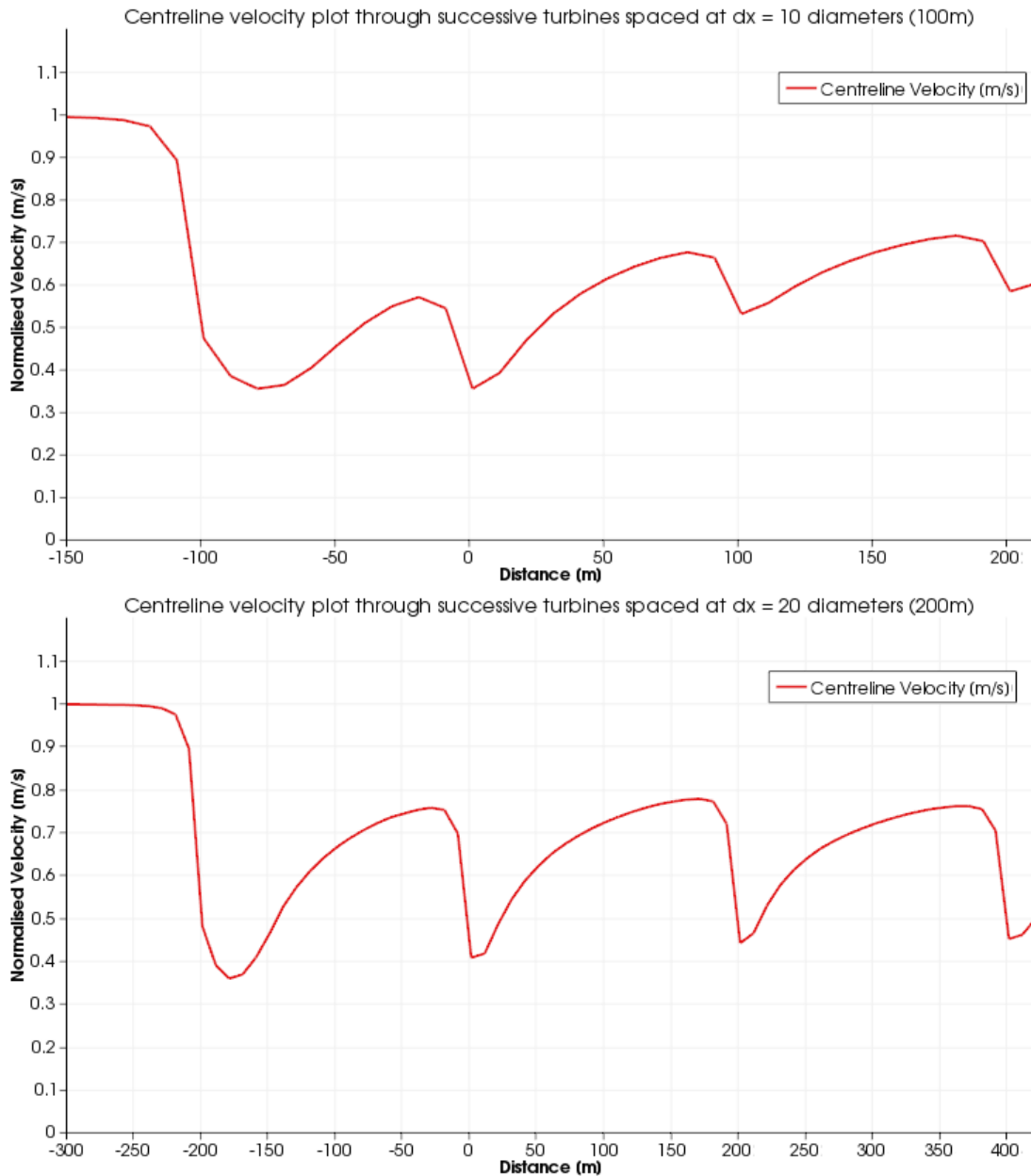
Figure 8: A plot of range normalised velocity along the centreline of the turbine array for different intervals. The top graph shows the centreline velocity recovery at turbine intervals of 10 diameters (100m). The bottom graph shows velocity recovery at 20 diameters (200m).

turbines due to the increased velocity at a given interval. From this the authors results show that a lateral spacing of two diameters is optimal for maximising power extraction. The work also shows that a downstream interval of seven diameters, in the two diameter lateral spacing case, provides the optimal spacing for power extraction in a finite total area. The work notes that the potential power extraction does not consider the effect on the flow a downstream turbine will have. In addition the cumulative effect of downstream turbines is not studied. The effect of different rates of momentum extraction by turbines, and thus wake deficit and recovery rate, is not examined. The authors state that turbines placed in the accelerated flow
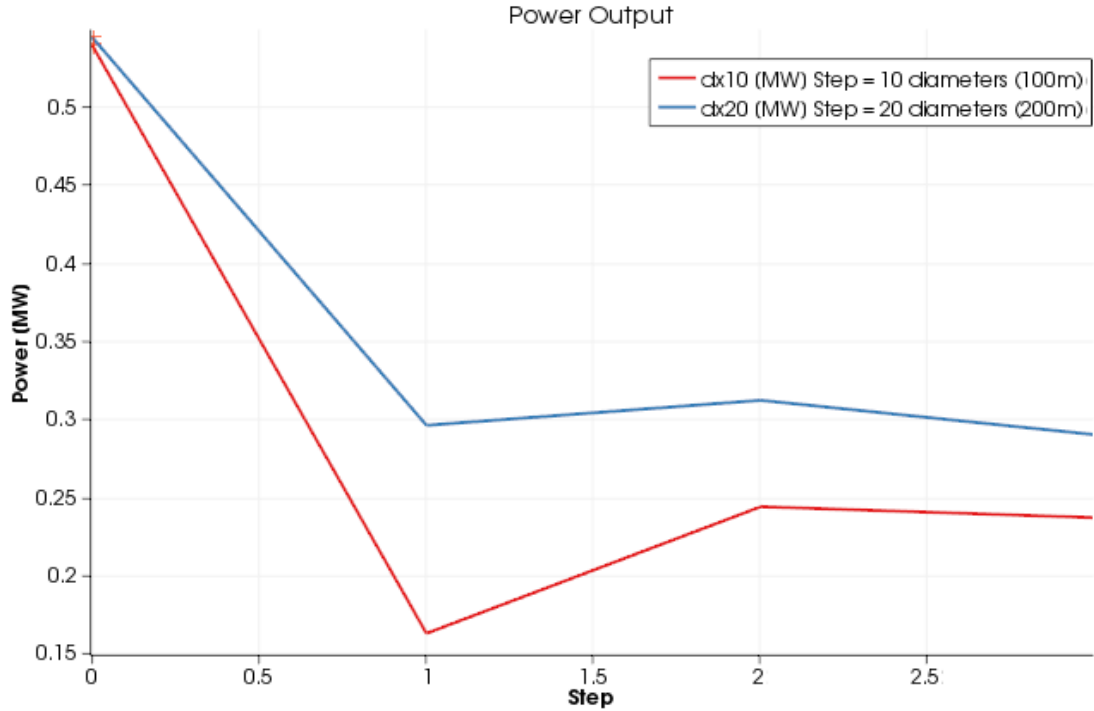
Figure 9: A plot of the power production of four turbines placed longitudinally at intervals of 10 and 20 diameters. The graph compares the results of both cases at the equivalent step (or interval) downstream.

| Turbine interval | 10 diameters (100m) [MW] | 20 diameters (200m) [MW] |
|---|---|---|
| First turbine | 0.539 | 0.544 |
| Second turbine | 0.163 | 0.296 |
| Third turbine | 0.244 | 0.312 |
| Fourth turbine | 0.237 | 0.290 |
| Total Power | 1.183 | 1.442 |

Figure 10: A tabulation of the total power of each array in Figure 9.

outside the wake regions could be exploited to increase the power extraction potential of a site. In our work we discuss how these considerations effect the potential power extraction when computing optimal turbine array density in a given area or site.

In our study we examine two scenarios; the first scenario is of 4 turbines situated downstream of each other in open flow at intervals of 10 diameters, the second scenario spaces the turbines at intervals of 20 diameters, see Figure 12. The objective is to extend the previous work by [24] and to consider the cumulative effect of multiple rows of turbines. The domain width is 20 diameters, which simulates (resembles) an open region of flow with minimal blockage. From this we expect a negligible increase in the free stream velocity of 3m/s in the bypass region of the turbines. Our experiments have highlighted that there is no significant difference in the bypass region with a domain width of six diameters and greater.

In the 20 diameter case it is observed that the average wake velocity recovery stabilises after approximately 16.5 diameters downstream (approx. 75% wake velocity recovery [17]), see Figure 12. Power generation also stabilises due to its relation to input velocity. After this interval the average wake velocity drop and recovery across the turbines spaced at 20 diameters becomes periodic, see Figure 8. The turbines spaced at intervals of 10 diameters do not initially recover to a stable state and continues to recover past the next turbine, see Figure 12 and 8. As a result of reduced velocity recovery, power production drops

for the second device. However, the recovery improves for the following devices. Figure 12 shows both turbulence and wake width increasing downstream due the increased disruption from the upstream devices. Increased turbulence, and thus momentum transfer in the wake region, improves the velocity recovery rate thus improving the power generation further downstream. These interactions within the wake region are more complex than suggested by [24].

Another important aspect of the shadowing of downstream turbines is power extraction. Obviously, the velocity deficit shadowing of downstream turbines also influences the power extraction of the array. In the two cases it is observed in Figure 9 and Table 10 that power extraction in the 10 diameter case initially drops but then recovers, while the 20 diameter case is fairly consistent. Although the device extraction efficiency in the 20 diameter case is better, the overall power extraction achieved by a more closely packed array for a given length or area would be significantly greater for the 10 diameter case.

### 4.3. Reduction of Computational Overhead

To get a result from a simulation of a large turbine array site with acceptable accuracy it may be required to remove some of the complexity from the mesh. One possibility is the removal of the tower and nacelle geometry thus simplifying the mesh and simulation. To simulate the tower and nacelle we would require a significant increase of the number of small cells in these areas to produce a reasonable convergence of the flow characteristics. We study the effect of removing these cells from the mesh on the results of the simulation, and consider the effect on power production.

Figure 13 shows a vertical slice through the flow along the centreline of a turbine assembly. The colour is mapped to velocity. The top simulation is with the turbine assembly, whereas the bottom is without. Comparing these slices provides us with a robust understanding of the velocity distribution within the downstream wake region, and the effect of removing the turbine assembly from the simulation. It can be clearly seen that there is a drop in velocity immediately behind the nacelle, expanding downstream around the centre of the wake region. This low velocity region dissipates by approximately 6 diameters downstream relative to the solution without tower and nacelle. The momentum transfer back into the wake occurs more quickly in the tower and nacelle solution as a result of the increased turbulence created by the nacelle. The increased turbulence is demonstrated in Figure 14 where a similar comparison of solutions are shown with colour mapped to turbulence intensity. At a distance greater than 6 diameters downstream the solution of the two cases converge. Placing turbines in the wake less than 6 diameters downstream will provide differing inlet velocities to the downstream turbine when not simulating the tower and nacelle providing potentially misleading results, i.e. inaccurate power production quantities for the downstream devices.

The tower also has a significant effect on the flow. In particular immediately downstream of the tower Figures 14 and 13 show a significant increase in turbulence, and reduction in velocity. Although this dissipates within approximately 2 diameters downstream, it causes a slight asymmetry to the downstream wake structure. The increased turbulence will likely have an impact on the local environment. The simulation with tower and nacelle provides an output of $0.584MW$, and without provides $0.591MW$. The performance of the rotor increases by about 1.2% where the tower and nacelle are neglected from the simulation. This phenomena is attributed to the additional velocity available at the centre of the blade area. This differences can be seen in Figure 15. The left image shows the blade area with tower and nacelle, and the right image shows additional velocity at the centre of the plot. The velocity distribution remains similar across the remainder of the blade area.

### 4.4. Transverse Contrarotation

The concept of transverse contrarotation and its influence on the wake region is studied to determine if there is a significant effect which would need to be considered when evaluating a given turbine array layout. Transverse contrarotation is a description of a lateral array of turbines each rotating in the opposite direction to its neighbour. In our case study we place one turbine at 1 diameter downstream and in between a pair of turbines separated by a distance of 1.5 diameters as can be seen in Figures 16. In the standard case the turbines all rotate the same clockwise direction when view from the direction of flow i.e. inlet. The two front turbines of the contrarotation case rotate in opposing directions. The front left and rear turbines rotate clockwise, and the front right rotates anticlockwise as viewed from upstream.

In Figure 16 we see a velocity plot of the wakes and their evolution downstream. The top image of the contrarotation case shows little variation compared with the standard rotation case. The distribution of velocity across the wake, and downstream doesn't significantly change, except for two important aspects. The first aspect is the upward motion of the low velocity region behind the centre wake of the contrarotation case as shown in Figure 17. This upwardly moving flow in the wake region is confirmed in Figure 19. The second important aspect is the location at one side of the rear turbine where the velocity drop is significantly less in the contrarotation case. The difference in this area can also be seen in Figure 18, where there is significantly less turbulence in the same location.

In the standard case, the rear turbine blade meets the wake swirl with a greater angle of attack and thus creates additional turbulence. Conversely the contrarotating rotor produces a wake which rotates in the opposite direction, thus the wake is meeting the rear blade at a smaller angle of attack generating less turbulence. The two wakes in this region are also rotating counter to each other generating less shear. This is more clearly illustrated in Figure 19 which shows how the wake rotations are working in unison for the contrarotation case. Although there is an asymmetry as compared to the standard rotation case, the power extraction results are the same for each turbine in both cases. The two front turbines generate an output of $0.573MW$, and the rear turbine an output of $0.396MW$.

*4.5. Headland Flow Blockage*

| | Blockage Ratio = 0.13 | | Blockage Ratio = 0.17 | | Blockage Ratio = 0.20 | |
|---|---|---|---|---|---|---|
| | Location | Power | Location | Power | Location | Power |
| 1 | -90 | 2.39 | -87.5 | 2.47 | -86 | 2.52 |
| 2 | -110 | 2.13 | -102.5 | 2.26 | -99 | 2.34 |
| 3 | -130 | 1.91 | -117.5 | 2.08 | -112 | 2.18 |
| 4 | -150 | 1.73 | -132.5 | 1.92 | -125 | 2.03 |
| 5 | -170 | 1.58 | -147.5 | 1.79 | -138 | 1.91 |
| 6 | -190 | 1.43 | -162.5 | 1.67 | -151 | 1.79 |
| 7 | | | -177.5 | 1.56 | -164 | 1.69 |
| 8 | | | -192.5 | 1.43 | -177 | 1.58 |
| 9 | | | | | -190 | 1.47 |
| Total | | 11.16 | | 15.19 | | 17.49 |
| Average | | 1.86 | | 1.90 | | 1.94 |

Table 1: A tabulation of the location and power output of each turbine for the range of turbine fence densities studied. The total power output, and per turbine average is recorded. Power is measured in Megawatts, and location in meters in the z axis direction from the headland centre.

To understand the effect of placing arrays of marine turbines close to a headland, it is useful to study the flow blockage caused by these turbines. [10] demonstrate a method for predicting potential power extraction over a full tidal cycle using a method similar to the classic actuator disc model expressed over a lateral fence. The fence is situated off the tip of the headland at a location capturing the maximum kinetic flux within the domain. The authors perform their simulations utilising a 2D mesh which represents a depth averaged domain. The authors describe a blockage ratio $B$ as the ratio of turbine area and channel area confined to the pitch of turbines in the lateral fence array. The blockage ratio is defined as follows:

$$B = \frac{A}{bh}$$

where A is the device area, b is the lateral pitch of devices, and h is the channel depth at the fence.

In our work we study the effects on flow within a 3D domain using the BEM-CFD model to determine if the characteristics observed in [10] are comparable. In our work we use a turbine of diameter $10m$ situated in a $30m$ channel at a location consistent with [10]. If the inter device pitch of the turbine fence array is
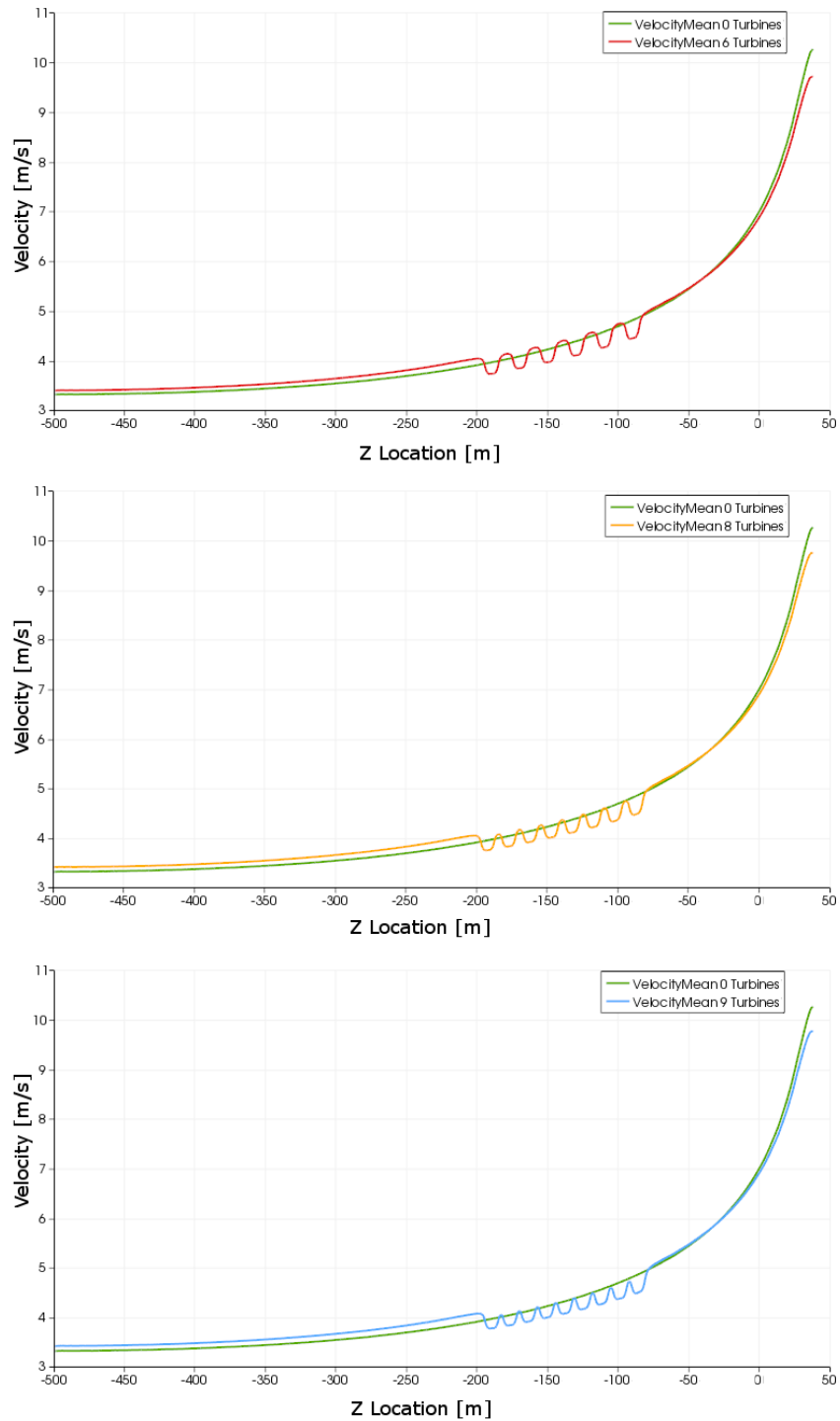
Figure 11: A comparison of depth averaged velocity profiles for different blockage ratios of tidal fences. A baseline depth averaged velocity profile without a tidal fence is shown in all three graphics. Fence blockage ratios of 0.13, 0.17, and 0.20 are equivalent to 6, 8, and 9 turbines respectively.

set at $10m$, i.e. neighbouring rotor blades are touching, the blockage ratio is determined as $B = 0.26$. This value is therefore the maximum theoretical blockage ratio within this combination of channel depth and rotor disc area. For our simulations we use 0.13, 0.17, and 0.20, which provide a more realistic density of devices in our study, as we do not simulate the sloping bathymetry of the coastline.

In our study we examine the characteristics of the flow passing through a predefined area of the domain. This area is a slice through the domain between the headland and open ocean boundary as shown in Figure 20. We compute depth averaged velocity along this vertical slice and show the results of the three blockage ratios and the base results without turbines. This is illustrated in Figure 11. We observe from these results an increase in the flow on the open ocean side of the domain when a turbine fence is realised. In the area between the headland and the turbine fence we see a reduction in velocity as compared to the base case. This behaviour is consistent with the findings of [10]. These characteristics are also observed in Figure 22 which show stream surfaces propagated through the flow and colour mapped to velocity. In Figure 22 a velocity gradient is observed across the turbine fence, and the accelerated flow can be seen in the bypass regions. The interaction of the individual turbines with the flow, and the flow bypass regions either side of each individual turbine is also observed.

The recirculation downstream of the headland can be seen clearly in Figure 21 for all four cases, and in Figure 22 for the 0.20 blockage ratio case. The most noticeable difference is between the baseline case and the three fence cases. The flow separation is located further around the headland, the velocity is significantly less, and the rotation of the flow is elongated along the coast in comparison to the fence cases. The flow separation and rotational flow past the headland is also highlighted in Figure 22. The addition of the turbine fence in all the configurations may have an impact on the local environment, in particular the sediment transport system. [2] postulate that the effect of small numbers of turbines may be less than annual variation in sediment movement due to storm effects. [10] notes the advection of transient eddies from the tip of their headland case most similar to Portland Bill, UK. However, the recirculation of flow behind the headland case in our studies is not transient, as our simulations are steady state. The seaward location of the eddies in [10] are due to the different bathymetry near the coastline, where the velocity reduces towards the coast as the frictional forces increase due to reduced depth. Our domain considers a constant depth across the sea bed, and doesn't factor in the sea bed rising towards the coastline.

Power extraction results from the three fence cases can be seen in Table 1. The table demonstrates a significant increase in power extraction at the southern end of the fence. [10] observed little variation across the fence, however the large variation across our results is likely due again to the difference in bathymetry near the coast. The maximum calculated kinetic flux shown in Figure 23 can clearly be seen at the tip of the headland. In the case of [10] their results show maximum kinetic flux situated away from the headland, whereas our results show the kinetic flux located at the tip of the headland, see Figure 23. This again is due to the differing bathymetry in the coastal region and explains the difference in power extraction across the turbine fence.

Table 1 shows the average power extraction rate increases as the density of turbines increase. This phenomena is attributed to the volume of flow through the fence area not changing thus total power potential increases with the use of more turbines. Figure 11 confirms that the bypass flow regions do not significantly change thus supporting this hypothesis.

## 5. Conclusions and Future Work

### 5.1. The Downstream Effect

When placing turbines downstream at intervals greater than 75% of the wake velocity recovery distance [17], i.e. 16.5 diameters in a free stream flow of 3m/s, the results demonstrate consistent wake recovery and thus consistent power extraction of downstream devices. This observation initially gives strength to the [24] hypothesis that the prediction of downstream power production can be achieved by applying a common factor to the power production at the upstream device. However, placing the turbines at intervals less than 75% of the wake velocity recovery distance [17], we note that the power production drops for the second device, while recovering for the following devices. This phenomena is due to the increased velocity recovery

rate resulting from increased turbulence, and thus momentum transfer, across the wake. This trend is not in line with the [24] hypothesis, suggesting a more complex set of interactions between downstream turbines. Further studies of this phenomena to strengthen our hypothesis, and to better understand the interactions at differing intervals is an interesting topic of future work.

### 5.2. The Lateral Fence Effect

Although [24] uses only one turbine, the simulation considered lateral pitches of 2 diameters to 6 diameters. This has a significant effect on the bypass velocity to maintain constant mass flow, i.e. it is significantly increased. A secondary effect of this is the increase in velocity gradients across the boundary of the wake, which in turn, due to increased shear stress, leads to more rapid momentum transfer back into the wake. This increases the rate of wake velocity recovery over the same period. Use of this velocity bypass region by staggering consecutive rows of turbines is studied by [19]. The work indicates that the relationships between consecutive rows is more complex than suggested by [24] and would require further investigation to prove such hypothesis.

### 5.3. The Tower and Nacelle Effect

The low velocity region immediately behind the nacelle dissipates by approximately 6 diameters downstream relative to the solution without tower and nacelle. At a distance greater than 6 diameters downstream the solution of the two cases converge. Placing downstream turbines in the wake less than 6 diameters will provide differing inlet velocities to the downstream turbine when not simulating the tower and nacelle. This could provide misleading results. [17] studies wake length and width at differing flow rates. The authors suggest that the relationship between length, width, and input velocity is not linear. It would be useful future work to understand, from a planning point of view, how this distance downstream changes with change in free stream velocity, or change in power absorption by the turbine assembly.

The tower also has an effect on the flow immediately downstream, in particular the sea bed. This has an effect on the local environment which may need to be considered if running simulations without the tower and nacelle. The performance of the turbine simulated without tower and nacelle increases by about 1.2% as compared to the solution with tower and nacelle. The additional velocity available at the centre of the blade area increases the simulated power output. An area of future work would be to run the simulations with a solid centre in place of the missing nacelle to confirm a more accurate solution to neglecting the tower and nacelle.

### 5.4. The Contra Rotating Effect

In the context of a time averaged simulation the interaction of the neighbouring or downstream wakes does not alter the extraction of power in the scenario of transverse contrarotation. An interesting effect of the contrarotation case is the reduced turbulence at the rear rotor. However, if the rotors of the rear turbines do not cross the wake boundaries this scenario may not occur. An interesting future work direction is a study of this phenomena within the context of opposed staggered contrarotating rows of turbines.

### 5.5. The Headland Effect

The headland study highlights some useful phenomena related to deployment of arrays in realistic channels. Although the case has one simple variation to a uniform cross section, the presence of the headland and the close spacing of the rotors leads to a number of flow features. The performance variation of the rotors is consistent with the velocity variation, and the results do show positive blockage leading to higher power output. The effect of the fence on the flow are also seen with the increased velocity of the bypass flow and the curved nature of the downstream wakes. It is important to note that for a given system the available power is related to the net drag of that system. For example; drag from the tower, nacelle and related structures will reduce the kinetic flux thus available power. Also, while the rate of momentum transfer into the wake increases with increased blockage, this will be at the cost of additional momentum loss. This reduction in flux will increase with the number of turbines at the site.

The addition of the turbine fence in all the configurations may have an impact on the local environment, in particular the sediment transport system. The characteristic increase in ocean flow, and reduction in headland bypass flow, due to the fence blockage is consistent with the findings of [10].

## 5.6. Operating Velocity of Downstream Devices

Manually setting the operating tip speed ratio of downstream devices can easily place them outside the optimum performance range. As a result the devices will do very little to extract energy from the flow. In the context of our simulations setting the correct parameters required an iterative approach of trial and error. There is a definite need to investigate an automated approach within the simulation system which can output the optimum device operation, and simulation results together.

## 5.7. Summary of Conclusions

There are a number of papers which examine different aspects of marine turbines providing new knowledge for the industry supporting successful deployment of arrays in differing ocean topographies. Our work pays attention to a range of differing aspects to further extend the current published works. We conclude that interactions between downstream turbines, and relationships between consecutive rows of turbines is more complex than suggested by [24]. The tower and nacelle geometry can be removed from the simulation to reduce the computation requirements provided the effects of the tower and nacelle on flow characteristics are understood. The effect of contrarotation on power generation is negligible, however the interaction between neighbouring wakes which overlap downstream turbine rotors may effect the amount of turbulence generated. In the headland case the general trend of flow characteristics is in line with [10]. However, location of optimal fence turbine array is very dependant on the local bathymetry close to the headland/coastline. This also effects the optimum fence packing density in this area maximising power extraction. Finally, we conclude that these simulations of aspects of the design of tidal turbine arrays will, in a small way, help the progress of marine renewable energy.

## References

[1] S. P. Neill, J. R. Jordan, S. J. Couch, Impact of tidal energy converter (tec) arrays on the dynamics of headland sand banks, Renewable Energy 37 (1) (2012) 387 – 397. doi:http://dx.doi.org/10.1016/j.renene.2011.07.003.
URL http://www.sciencedirect.com/science/article/pii/S0960148111003855

[2] M. Lewis, S. Neill, The importance of waves within assessing the impact of tidal energy schemes, in: Proceedings of the 10th European Wave and Tidal Energy Conference, 2013.

[3] W. Batten, A. Bahaj, A. Molland, J. Chaplin, Experimentally validated numerical method for the hydrodynamic design of horizontal axis tidal turbines, Ocean Engineering 34 (7) (2007) 1013–1020.

[4] A. Bahaj, A. Molland, J. Chaplin, W. Batten, Power and thrust measurements of marine current turbines under various hydrodynamic flow conditions in a cavitation tunnel and a towing tank, Renewable energy 32 (3) (2007) 407–426.

[5] T. Stallard, R. Collings, T. Feng, J. Whelan, Interactions between tidal turbine wakes: experimental study of a group of three-bladed rotors, Philosophical Transactions of the Royal Society A: Mathematical, Physical and Engineering Sciences 371 (1985).

[6] D. O'Doherty, A. Mason-Jones, T. O'Doherty, C. Byrne, I. Owen, W. Wang, Considerations of improved tidal stream turbine performance using double rows of contra-rotating blades, in: Proceedings of the 8th European Wave and Tidal Energy Conference. Uppsala, Sweden: IET Renewable Power Generation, 2009, pp. 434–442.

[7] J. McNaughton, S. Rolfo, D. D. Apsley, T. Stallard, P. K. Stansby, "cfd power and load prediction on a 1mw tidal stream turbine with typical velocity profiles from the emec test site", in: Proceedings of the 10th European Wave and Tidal Energy Conference., 2013.

[8] J. Banks, K. Bercin, T. P. Lloyd, S. R. Turnock, Fluid structure interaction analyses of tidal turbines.

[9] T. Nishino, R. Willden, Two-scale dynamics of flow past a partial cross-stream array of tidal turbines, Journal of Fluid Mechanics (2013) 220–244.

[10] S. Draper, A. Borthwick, G. Houlsby, Energy potential of a tidal fence deployed near a coastal headland, Philosophical Transactions of the Royal Society A: Mathematical, Physical and Engineering Sciences 371 (1985).

[11] R. Mikkelsen, J. N. Sørensen, S. Øye, N. Troldborg, Analysis of power enhancement for a row of wind turbines using the actuator line technique, in: Journal of Physics: Conference Series, Vol. 75, IOP Publishing, 2007, p. 012044.

[12] R. Malki, A. Williams, T. Croft, M. Togneri, I. Masters, A coupled blade element momentum-computational fluid dynamics model for evaluating tidal stream turbine performance, Applied Mathematical Modelling.

[13] M. Harrison, W. Batten, A. Bahaj, A blade element actuator disc approach applied to tidal stream turbines, in: OCEANS 2010, IEEE, 2010, pp. 1–8.

[14] W. M. Batten, M. Harrison, A. Bahaj, Accuracy of the actuator disc-rans approach for predicting the performance and wake of tidal turbines, Philosophical Transactions of the Royal Society A: Mathematical, Physical and Engineering Sciences 371 (1985).

[15] N. Croft, K. Pericleous, M. Cross, Physica: a multiphysics environment for complex flow processes, Numerical methods in laminar and turbulent flow 9 (Pt 2) (1995) 1269–1280.

[16] R. Griffiths, M. Woollard, Performance of the optimal wind turbine, Applied Energy 4 (4) (1978) 261–272.

[17] R. Malki, I. Masters, A. Williams, T. Croft, The variation in wake structure of a tidal stream turbine with flow velocity, in: MARINE 2011, IV International Conference on Computational Methods in Marine Engineering, Springer, 2011, pp. 137–148.

[18] I. Masters, R. Malki, A. J. Williams, T. N. Croft, The influence of flow acceleration on tidal stream turbine wake dynamics: A numerical study using a coupled bem-cfd model, Applied Mathematical Modelling.

[19] R. Malki, I. Masters, A. J. Williams, T. Nick Croft, Planning tidal stream turbine array layouts using a coupled blade element momentum–computational fluid dynamics model, Renewable Energy 63 (2014) 46–54.

[20] L. Myers, A. Bahaj, An experimental investigation simulating flow effects in first generation marine current energy converter arrays, Renewable Energy 37 (1) (2012) 28–36.

[21] M. Edmunds, R. Laramee, R. Malki, I. Masters, T. Croft, G. Chen, E. Zhang, Automatic Stream Surface Seeding: A Feature Centered Approach, Computer Graphics Forum 31 (3.2) (2012) 1095–1104. doi:10.1111/j.1467-8659.2012.03102.x. URL http://dx.doi.org/10.1111/j.1467-8659.2012.03102.x

[22] M. Edmunds, R. S. Laramee, B. Evans, G. Chen, Stream Surface Placement for a Land Speed Record Vehicle, Tech. rep., The Visual and Interactive Computing Group, Computer Science Department, Swansea University, Wales, UK, (available online) (2013).

[23] M. Edmunds, R. S. Laramee, R. Malki, I. Masters, G. Chen, E. Zhang, Interactive Stream Surface Placement: A Hybrid Clustering Approach Supported By Tree Maps, 2014.

[24] S. R. Turnock, A. B. Phillips, J. Banks, R. Nicholls-Lee, Modelling tidal current turbine wakes using a coupled rans-bemt approach as a tool for analysing power capture of arrays of turbines, Ocean Engineering 38 (11) (2011) 1300–1307.

[25] B. E. Launder, D. B. Spalding, Lectures in Mathematical Models of Turbulence: By BE Lauder and DB Spalding, Academic press, 1972.
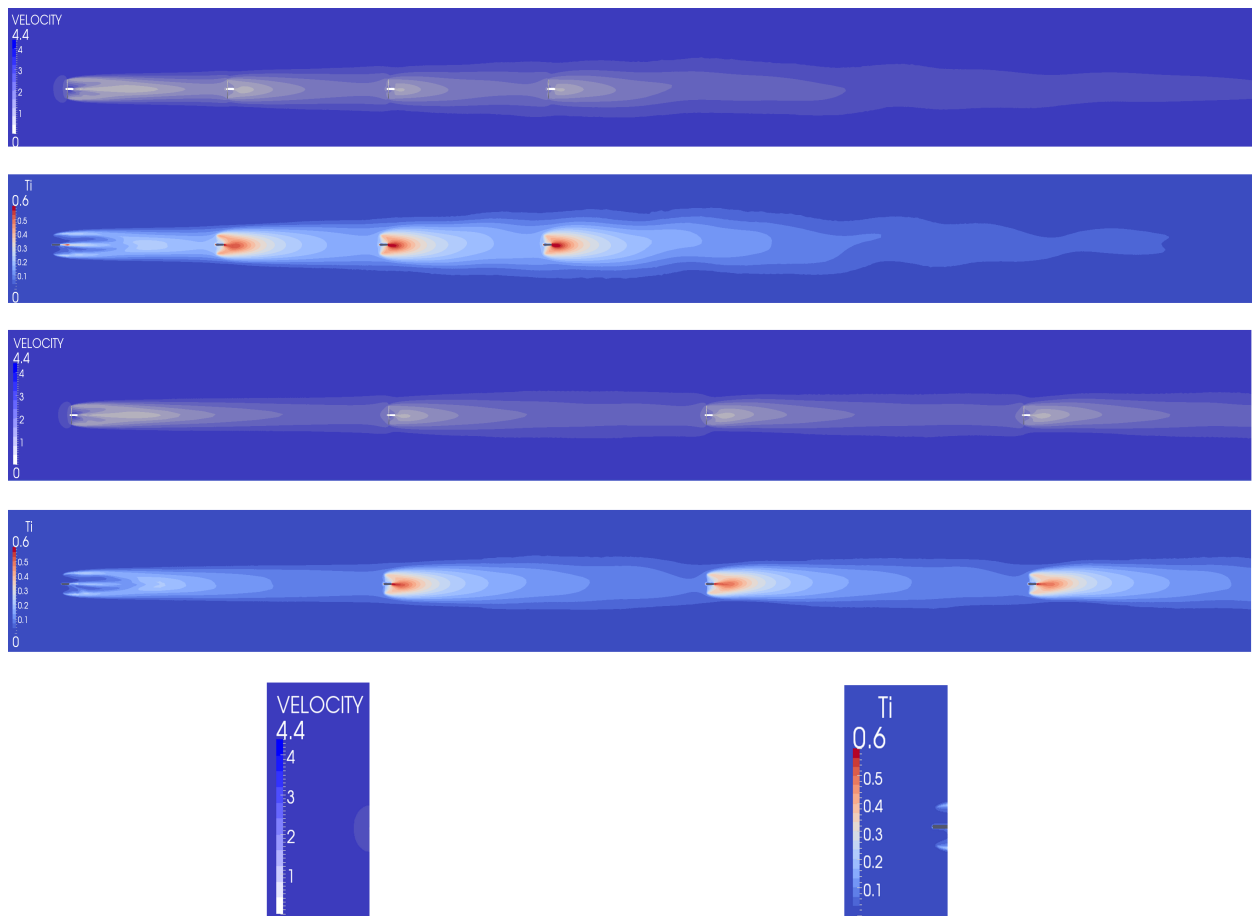
Figure 12: A comparison of velocity and turbulence intensity for a set of four turbines, each positioned downstream from each other. The first and second images show velocity and turbulence intensity respectively, at intervals of 10 diameters (100m). The third and fourth images again show velocity and turbulence intensity respectively, at intervals of 20 diameters (200m).
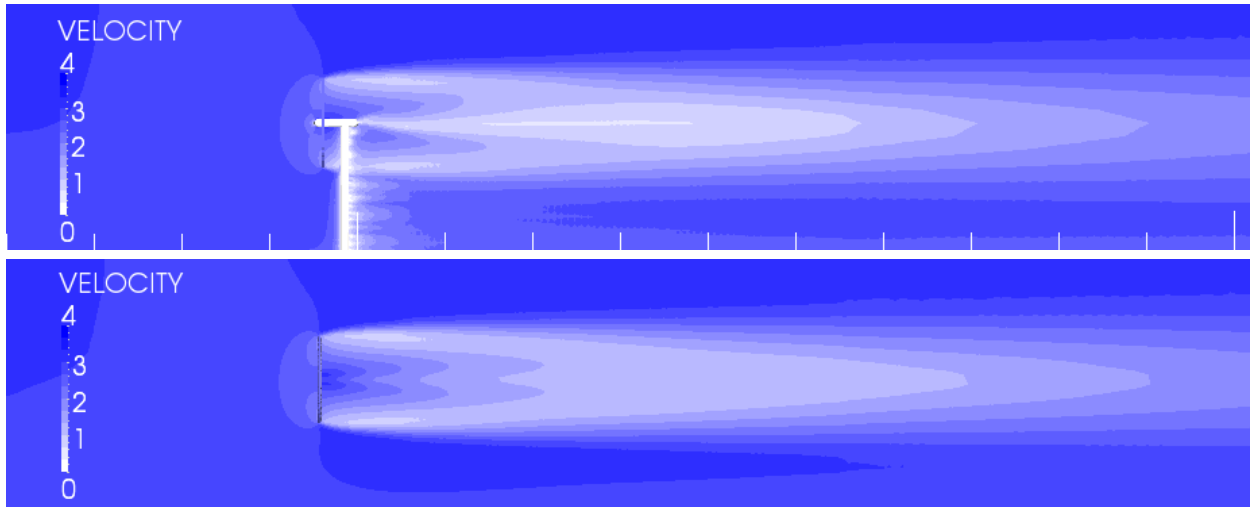
Figure 13: A comparison of velocity profiles downstream of the turbine rotors, with and without the tower and nacelle. The top image shows the results with the tower and nacelle, while the bottom image demonstrates the wake velocity difference when the tower and nacelle are omitted. The marking shown between the images show distance in multiples of the turbine diameter (10 meters).
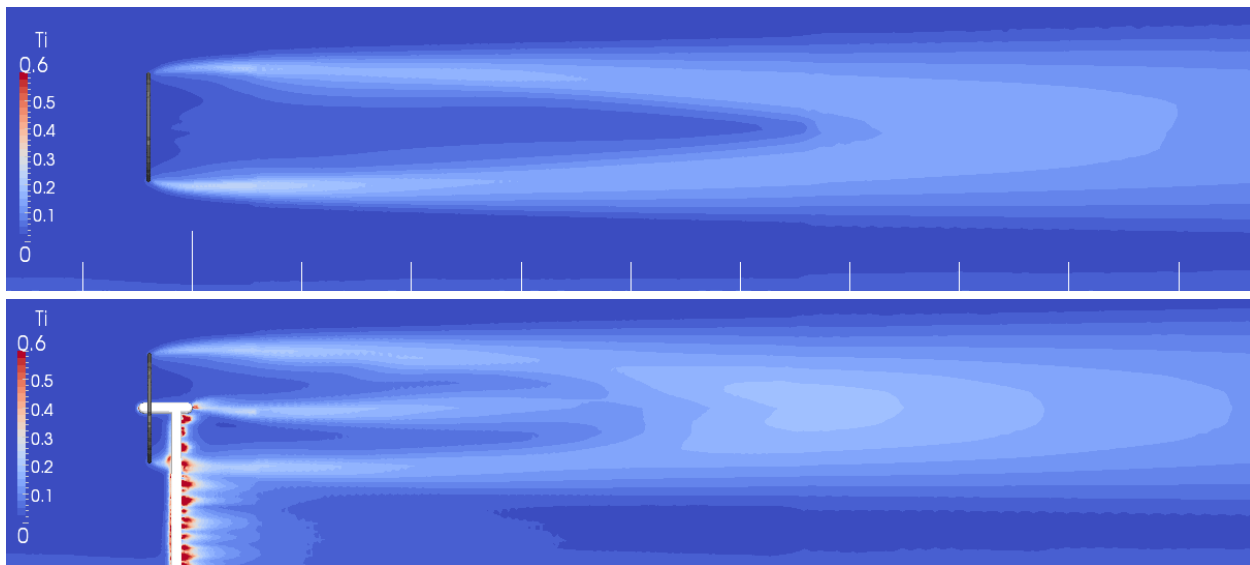


Figure 14: A comparison of turbulence intensity profiles downstream of the turbine rotors, with and without the tower and nacelle. The bottom image shows the results with the tower and nacelle, while the top image demonstrates the turbulence intensity difference when the tower and nacelle are omitted. The marking shown at the bottom of the images show distance in multiples of the turbine diameter (10 meters).
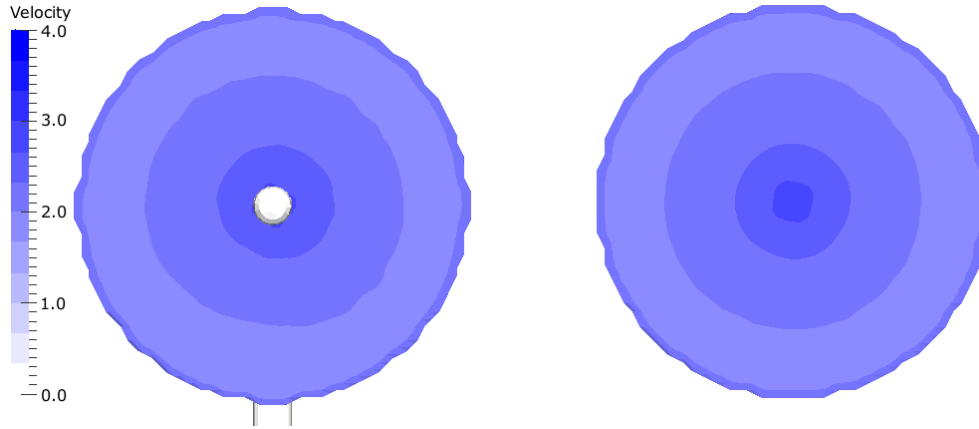
Figure 15: A depiction of velocity profiles across the blade area of the turbine. The top image highlights the velocity profile with tower and nacelle, while the bottom image demonstrates the velocity profile without the tower and nacelle.
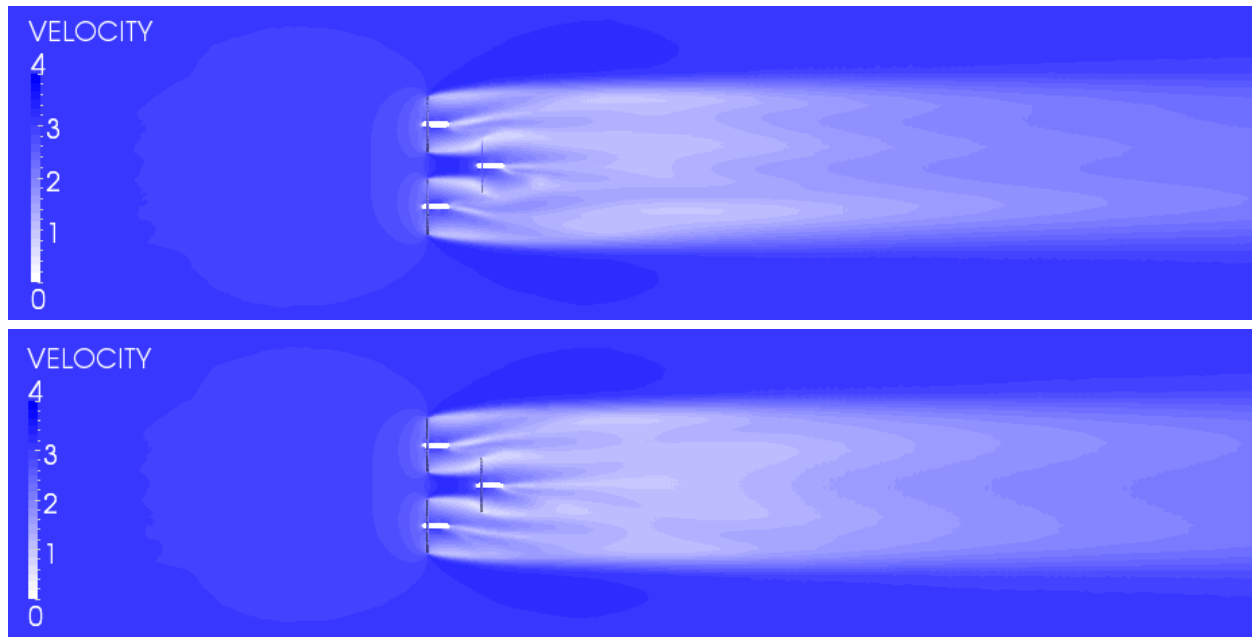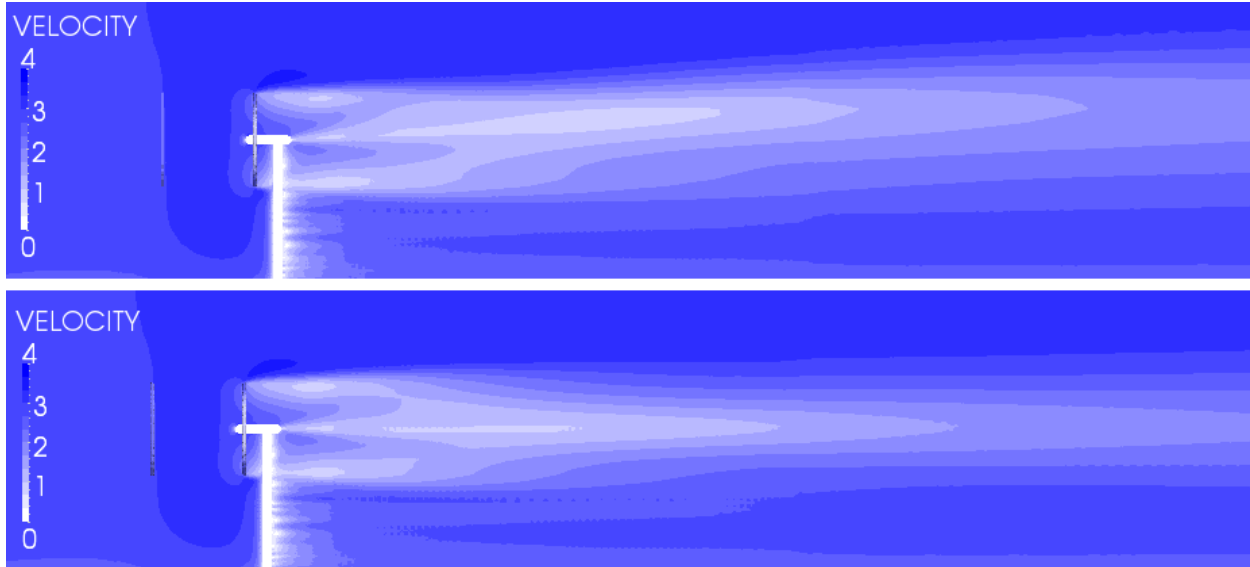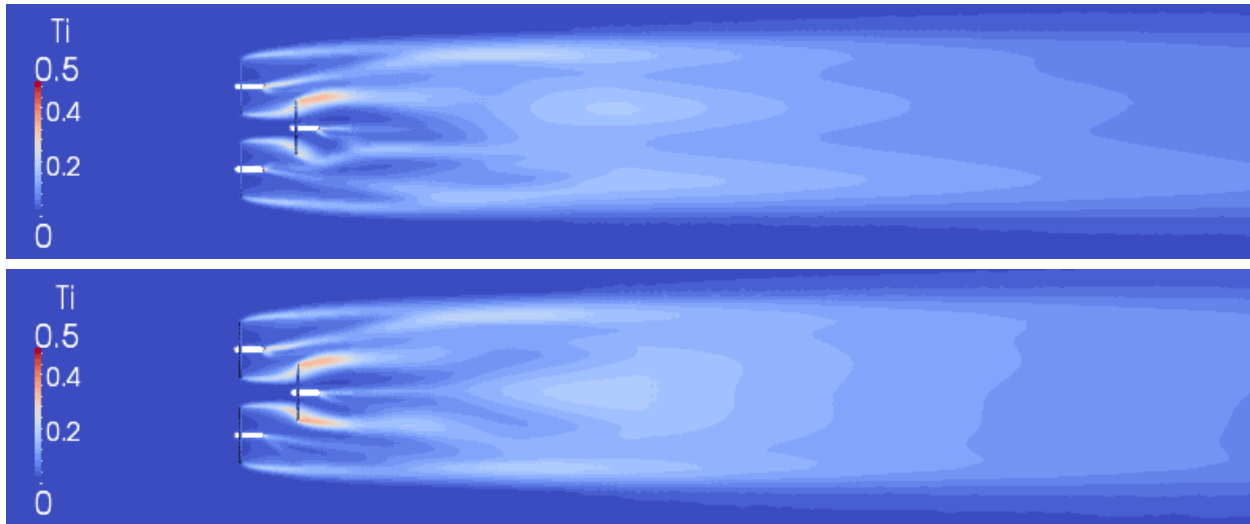


Figure 16: A comparison of the velocity profiles downstream of the turbine rotors. A horizontal slice is taken through the solution at nacelle centre hight. The top image shows the results of the transverse contrarotating case. The bottom image demonstrates the non contrarotating case.
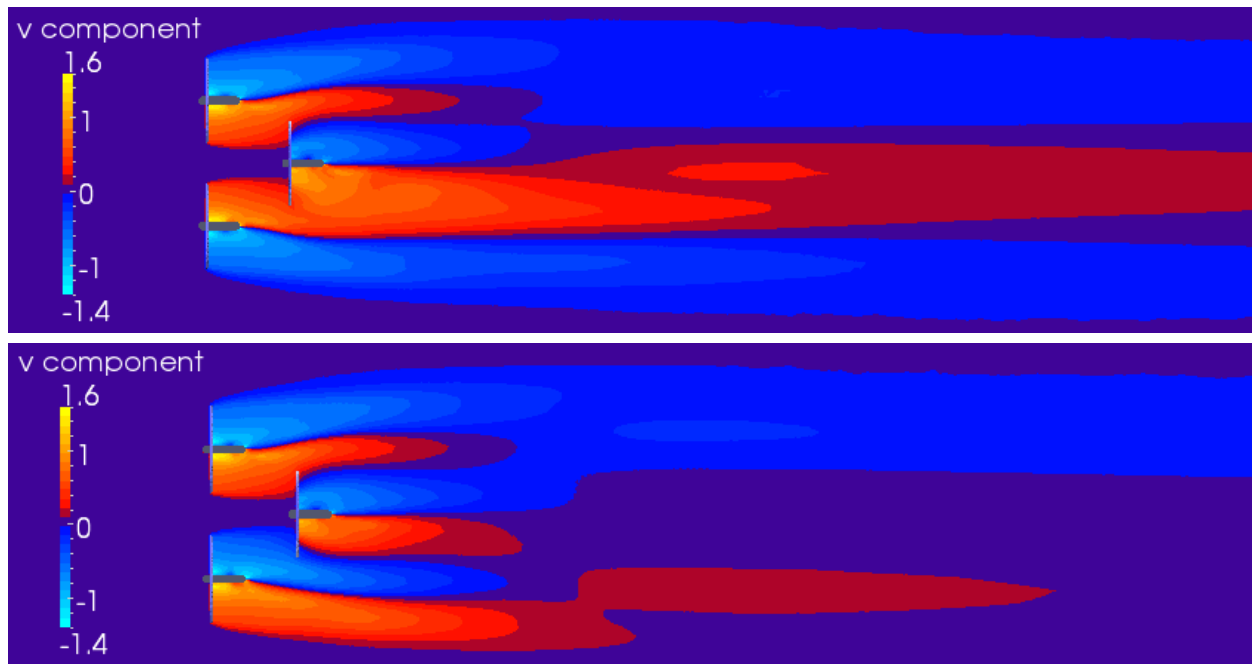
Figure 17: A comparison of the velocity profiles downstream of the turbine rotors. A vertical slice is taken through the solution at the centre turbine. The top image shows the results of the transverse contrarotating case. The bottom image demonstrates the non contrarotating case.



Figure 18: A comparison of the turbulence intensity profiles downstream of the turbine rotors. A horizontal slice is taken through the solution at nacelle centre hight. The top image shows the results of the transverse contrarotating case. The bottom image demonstrates the non contrarotating case.

Figure 19: A comparison of the up velocity component profiles downstream of the turbine rotors. A horizontal slice is taken through the solution at nacelle centre hight. Colour is mapped to the up component of velocity. The red scale is up, and the blue scale is down. The top image shows the results of the transverse contrarotating case. The bottom image demonstrates the non contrarotating case.
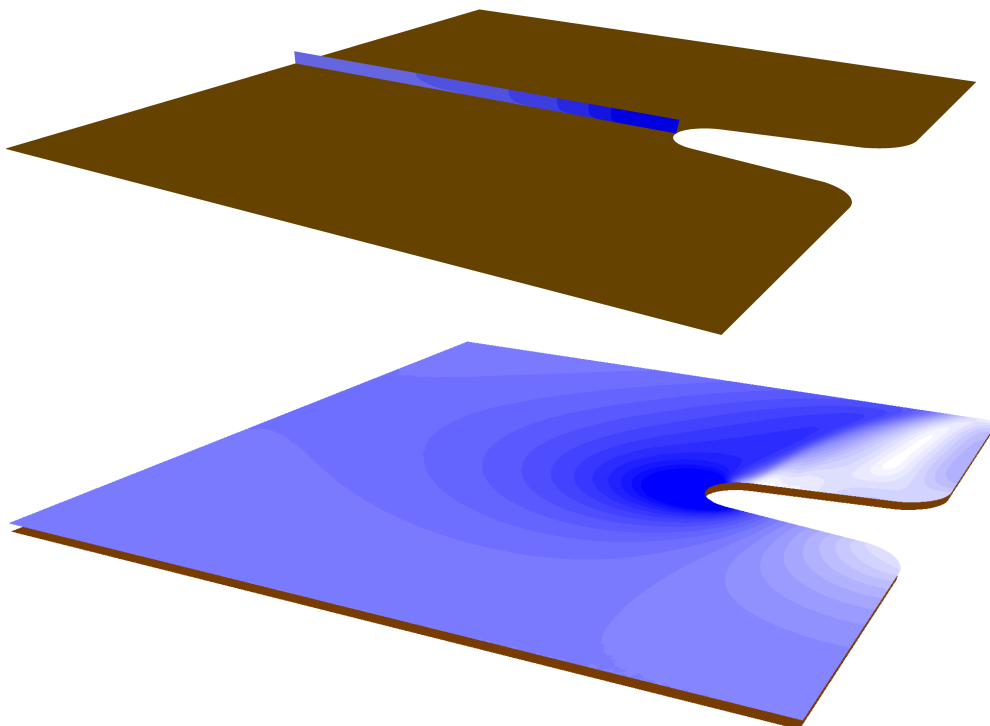


Figure 20: Spacial variation of velocity in the headland case. The velocity slice is colour mapped blue to white, while the sea bed is coloured brown. The top slice is located at the tidal fence, between the headland and the open sea. The bottom slice is taken at hub height across the domain.
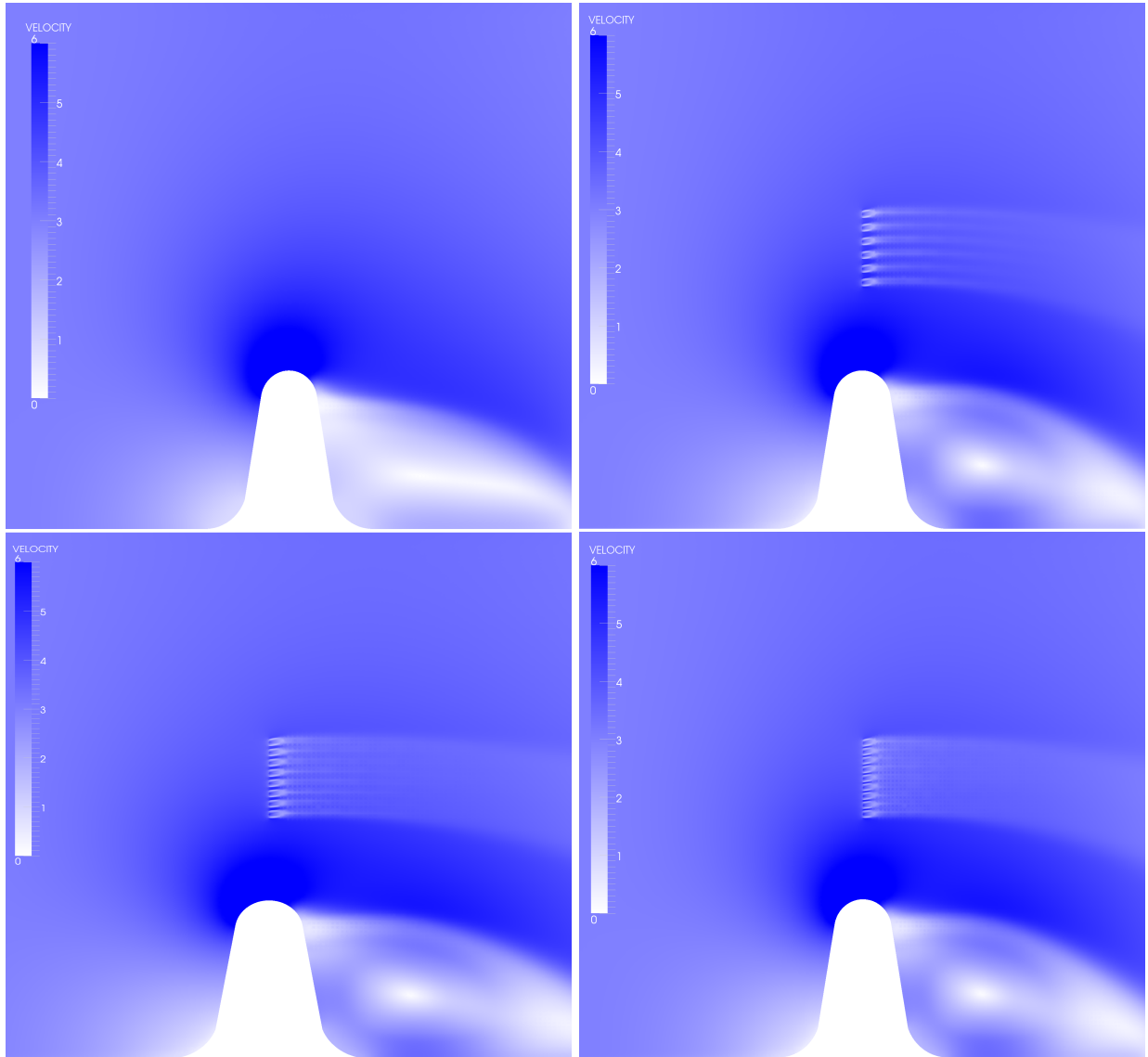
Figure 21: A comparison of the four headland cases from left to right, top to bottom; no turbine fence (baseline condition), turbine fence blockage ratio 0.13 (6 rotors), turbine fence blockage ratio 0.17 (8 rotors), and turbine fence blockage ratio 0.20 (9 rotors). The top images illustrate a velocity slice at rotor centre depth. The bottom images show streamlines seeded at the domain inflow.
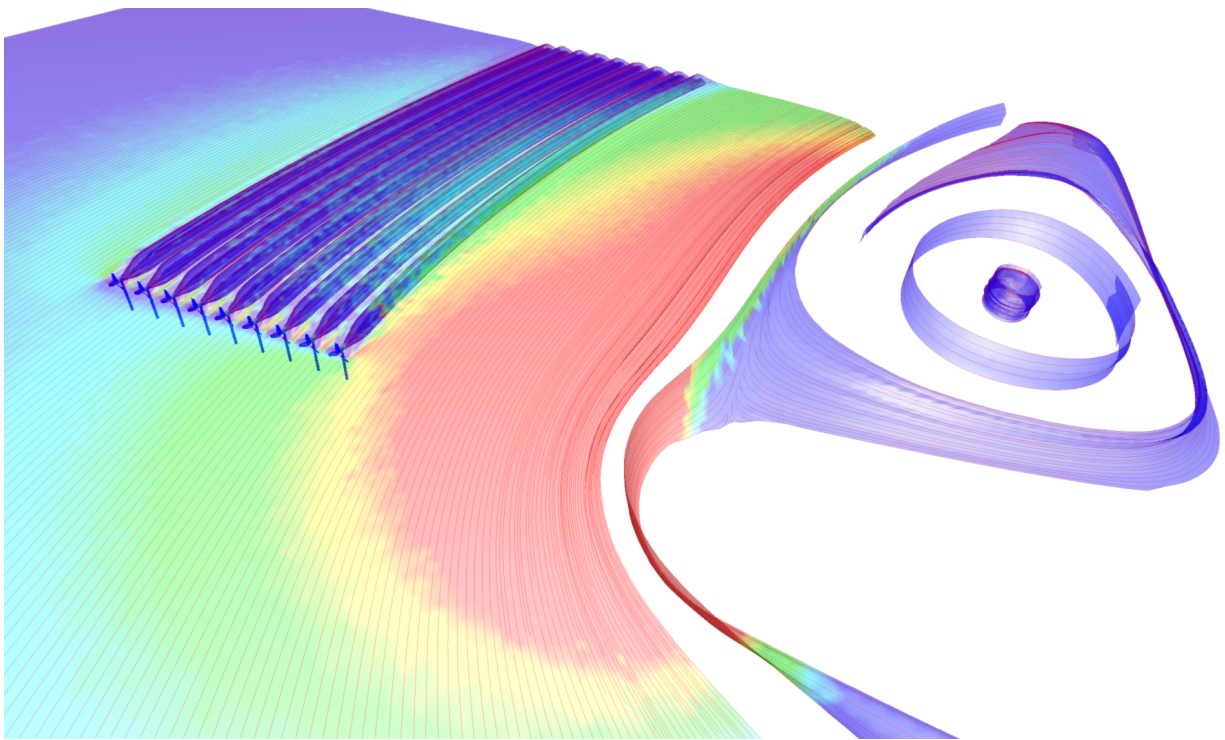
Figure 22: Stream surfaces showing the range of flow characteristics observed in 20, 11, and 21. The colour is mapped to velocity, and the surfaces are rendered with streamlines providing a visual cue of flow direction.
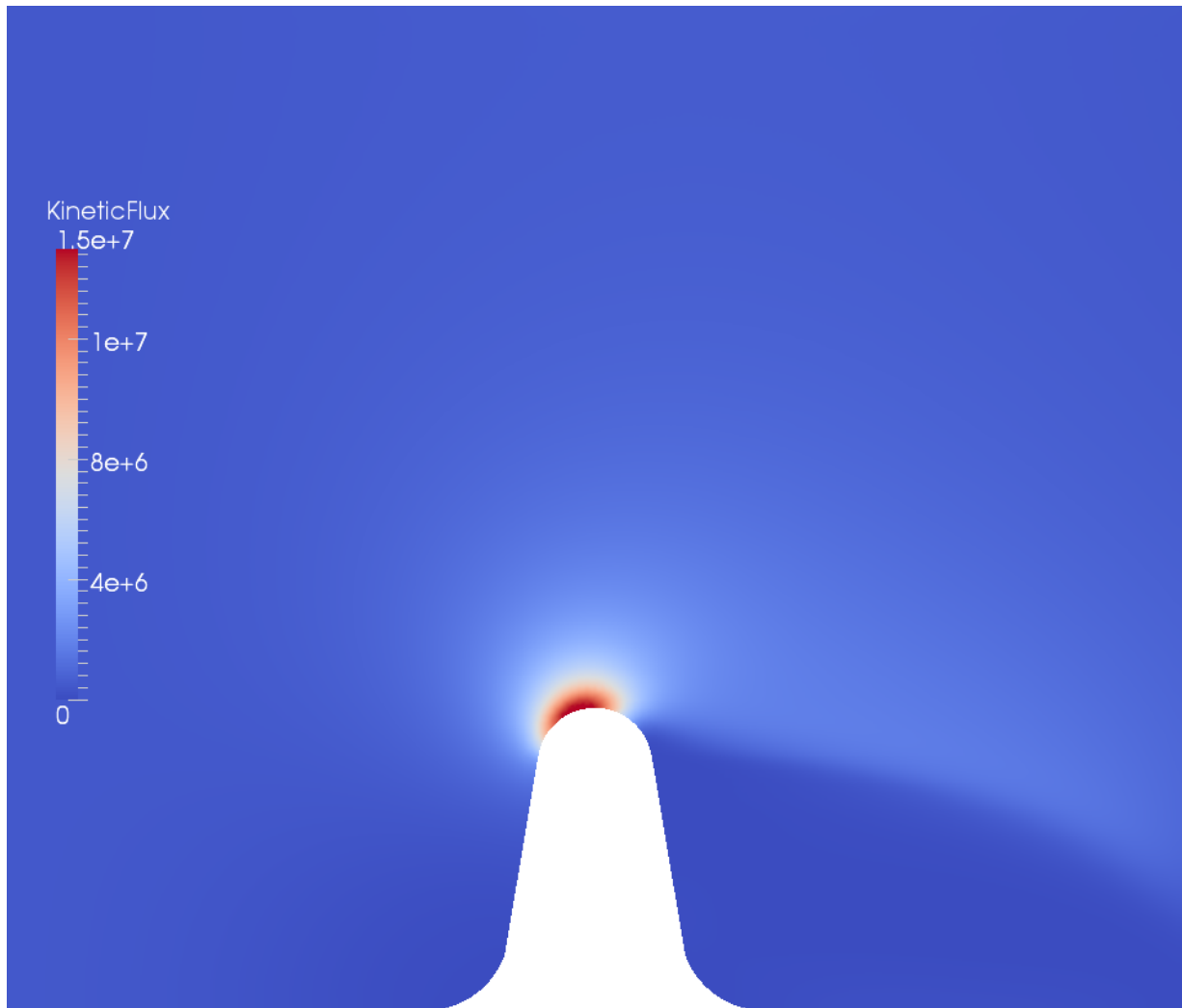
Figure 23: A slice through the centre of the domain colour mapped to kinetic flux. The Kinetic Flux is defined as $0.5\rho|u|^3h$ where $u$ is the local velocity, $\rho$ is density, and $h$ is the local channel depth.